Modeling multiscale necrotic and calcified tissue biomechanics in cancer patients: application to ductal carcinoma in situ (DCIS)

Paul Macklin*, Shannon Mumenthaler, and John Lowengrub

* Corresponding author: Paul.Macklin@usc.edu

URL: http://www.MathCancer.org/Publications.php#macklin12_springer

BibTeX Citation:

```
@incollection{macklin12_springer,
 author="Macklin, Paul and Mumenthaler, Shannon and Lowengrub, John",
 title="Modeling multiscale necrotic and calcified tissue biomechanics in cancer
        patients: application to ductal carcinoma in situ ({DCIS})",
 booktitle="Multiscale Computer Modeling in Biomechanics and Biomedical Engineering",
 editor="Gefen, Amit",
 chapter=8,
 year="2012 (accepted)",
 publisher="Springer",
 address="Berlin, Germany",
 note="(invited author: P. Macklin)",
}
```

EndNote Citation:
http://www.mathcancer.org/RIS_bookchapter.php?key=macklin12_springer

Modeling multiscale necrotic and calcified tissue biomechanics in cancer patients: application to ductal carcinoma in situ (DCIS)

Paul Macklin, Shannon Mumenthaler, and John Lowengrub

Abstract Tissue necrosis and calcification significantly affect cancer progression and clinical treatment decisions. Necrosis and calcification are inherently multi-scale processes, operating at molecular to tissue scales with time scales ranging from hours to months. This chapter details key insights we have gained through mechanistic continuum and discrete multiscale models, including the first modeling of necrotic cell swelling, lysis, and calcification. Among our key findings: necrotic volume loss contributes to steady tumor sizes but can destabilize tumor morphology; steady necrotic fractions can emerge even during unstable growth; necrotic volume loss is responsible for linear ductal carcinoma in situ (DCIS) growth; fast necrotic cell swelling creates mechanical tears at the perinecrotic boundary; multiscale interactions give rise to an age-structured, stratified necrotic core; and mechanistic, patient-calibrated DCIS modeling allows us to assess our working biological assumptions and better interpret pathology and mammography. We finish by outlining our integrative computational oncology approach to developing computational tools that we hope will one day assist clinicians and patients in their treatment decisions.

1 Introduction

At its most basic level, cancer is a disease of uncontrolled cell proliferation: cancer cells, either through mutations or epigenetic alterations, overexpress oncogenes and underexpress tumor suppressor genes (TSGs). Consequently, the cells enter into and progress through the cell cycle more often than they should and disregard apoptotic

Paul Macklin (invited author, corresponding author) and Shannon Mumenthaler
Center for Applied Molecular Medicine, Keck School of Medicine, University of Southern California, Los Angeles, CA USA   e-mail: Paul.Macklin@usc.edu   http://MathCancer.org

John Lowengrub
Departments of Mathematics, Chemical Engineering and Materials Science, and Biomedical Engineering, University of California, Irvine, CA USA   http://math.uci.edu/∼lowengrb

signals, resulting in a net increase in proliferation and aberrant tissue growth. (See recent cancer biology tutorials for modelers and physical scientists, such as [50, 52, 53].) Accordingly, cell proliferation and apoptosis, along with genetic mutations and epigenetic alterations in genes controlling these processes, have been major foci of both basic cancer research and modeling. Most cancer therapies attempt to manipulate these processes either by cytostatic (suppressing entry to or progression through the cell cycle) or cytotoxic (inducing apoptosis: programmed cell death) mechanisms. For example, chemotherapy agents such as doxorubicin are considered to be cytotoxic [10]; therapies that target hormone-addicted cells (e.g., tamoxifen in estrogen-driven breast cancer) are considered to be cytostatic [74].

Key biological and clinical terms

basement membrane (BM)	($\approx$100 nm) thick plasto-viscoelastic membrane separating epithelial and stromal tissues
extracellular matrix (ECM)	fibrous supportive scaffolding in stromal tissue
oncogene	a growth-promoting gene
tumor suppressor gene (TSG)	a growth-inhibiting gene
apoptosis	well-regulated, programmed cell death
anoikis	apoptosis due to loss of attachment to the BM
necrosis	disordered cell death
oncosis	cell death at the start of (or preceding) necrosis, marked by rapid cell swelling
adenosine triphosphate (ATP)	the immediate product of aerobic cell metabolism, and the "currency" of cell energy
(apoptotic) caspase	proteases responsible for degrading intracellular proteins during apoptosis
in situ carcinoma	cancer contained by an intact BM
ductal carcinoma in situ (DCIS)	an *in situ* precursor to invasive ductal breast cancer
comedonecrosis	necrotic tissue filling the lumen of a gland, most typically with intraductal breast cancers
invasive ductal carcinoma (IDC)	an invasive breast cancer derived from ductal cells
Van Nuys Prognostic Index (VNPI)	a system for evaluating DCIS and guiding treatment

Necrosis–the disorderly death of cells due to rapid injury or energy depletion—has seen less attention in basic cancer research and computational modeling. Indeed, cancer apoptosis publications outnumber cancer necrosis in PubMed by over three to one after excluding tumor necrosis factor (TNF) citations that are more directly related to apoptotic signaling than necrosis. Many prominent mathematical models do not incorporate necrosis (e.g., [8]), while others generically model cell death while failing to differentiate between apoptosis and necrosis. For example, the recent ductal carcinoma in situ (DCIS) model in [83] provided an excellent model of cell death due to energy depletion, but the work did not differentiate this death process (necrosis) from death due to detachment from the basement membrane (anoikis). As we shall see below, apoptosis and necrosis take widely divergent courses, particularly in cases of DCIS that exhibit *comedo*necrosis (necrosis filling the lumen of a gland).

Those models that do include necrosis have often modeled it as an instantaneous or fast time scale process by immediately removing necrotic cells from the simulations (e.g., [2]). Others have modeled necrosis as simple volume loss terms in continuum models (e.g., [12, 89, 90]), or as inert, persistent debris in discrete models (e.g., [21, 71]). While these are more true to the generally longer time scale of necrosis, they still fail to account for the multiscale processes involved and their potential biomechanical impact on tumor progression. None of these or other prior works have examined calcification of necrotic debris.

And yet necrosis plays a prominent, essential role in many carcinomas. A 1 mm tumor spheroid with a typical 100 μm viable rim is over 50% necrotic by volume. Cell death in such a significant fraction drastically alters mass transport throughout a tumor and can lead to steady size dynamics as proliferative cell flux out of the viable rim balances with fluid flux released by degrading necrotic cells [13, 50, 52]. See Fig. 1(left). Necrosis has a proven prognostic value in breast cancer, particularly ductal carcinoma in situ (DCIS) [72, 92]: presence or absence of comedonecrosis is a prominent part of the Van Nuys Prognostic Index (VNPI) [84]. Moreover, DCIS is primarily detected as subtle patterns of calcified necrotic tissue in mammograms [27, 29, 82]. See Fig. 1(right). 90% of all cases of nonpalpable DCIS are detected and diagnosed on the basis of microcalcifications alone [69]. Prominent tissue necrosis is also observed in other cancer types and can similarly be an important prognostic indicator [76], such as in glioblastoma multiforme [1, 70] and colorectal cancer [77]. Secretions by necrotic cells may promote inflammation in neighboring "normal" tissue (tumor-associated stroma) [9, 24, 31], thereby promoting progression from *in situ* to invasive carcinoma [26, 37, 79].

In this chapter, we shall explore recent efforts by our modeling groups to shed light on the impact of necrotic tissue biomechanics on tumor progression through increasingly sophisticated computational modeling. After a brief introduction in Section 2 to the biological background of apoptosis, necrosis, and calcification, we examine our earliest continuum-scale modeling of necrotic tumor growth [51, 58–62] in Section 3. Continuum conservation laws describe the biomechanics, while smaller scales are integrated as constitutive relations. The work gave early and extensive insights on the impact of necrotic core biomechanics on tumor growth, characteristic features, sizes, morphology, and stability.

In Section 4, we present a multiscale agent-based cell model [56] by Macklin and colleagues and apply it to ductal carcinoma in situ. The model is the first to incorporate the vast range of time scales of necrosis and calcification; tissue-scale biomechanics emerge from interactions among time-varying forces, adhesion characteristics, and individual cell volumes. This work, which included the first patient-specific calibration to pathology, gave new mechanistic insights on the impact of multiscale necrotic and calcified tissue biomechanics on features observed in patient pathology and mammography. We conclude by discussing the next steps in multiscale modeling of necrotic and calcified tissues, and we outline our vision for the future of clinically-focused *integrative computational oncology*. It is our belief that integrative modeling will increasingly push the envelope to advance the state-of-the-art across biology, engineering, mathematics, computing, and the clinical sciences.

2 Biological background

2.1 Basic biology of apoptosis

Apoptosis is a tightly-regulated, energy-consuming process [25, 36] that begins when intrinsic or extrinsic signals activate *initiator caspases* (e.g., Caspase-9) in the cytoplasm [25, 38]. This is generally regulated in one of two ways. In the first, mitochondrial membranes are permeabilized and release cytochrome c and other proteins into the cytoplasm to activate the initiator caspases. In the second, pro-apoptotic signals directly activate the initiator caspases independently of the mitochondria [38]. Mitochondria-regulated apoptosis disrupts ATP (energy) production by decreasing the mitochondrial membrane potential. The cell's remaining ATP store is depleted by energy-intensive processes throughout apoptosis [80]. See [65, 80] for greater detail on early regulation of apoptosis. While we do not describe them here, there are also caspase-independent apoptosis mechanisms [25, 38].

After apoptosis is initiated, various ion pumps on the cell's surface quickly remove water from the cell, resulting in significant volume loss [6, 14, 65, 67]. See Fig. 2(top:a-b) and Fig. 2(bottom). Indeed, cell shrinkage and separation from neighboring cells are some of the first visible signs of apoptosis in histopathology. The initiator caspases cleave and activate *effector* caspases (e.g., Caspase-3), which degrade cellular proteins [25, 38]. The cytoplasm collects in bulbous "blebs" that are shed from the cell. See Fig. 2(top:c). These blebs surround cell protein fragments with intact membrane, and thus typically do not trigger inflammation [25, 44, 65].
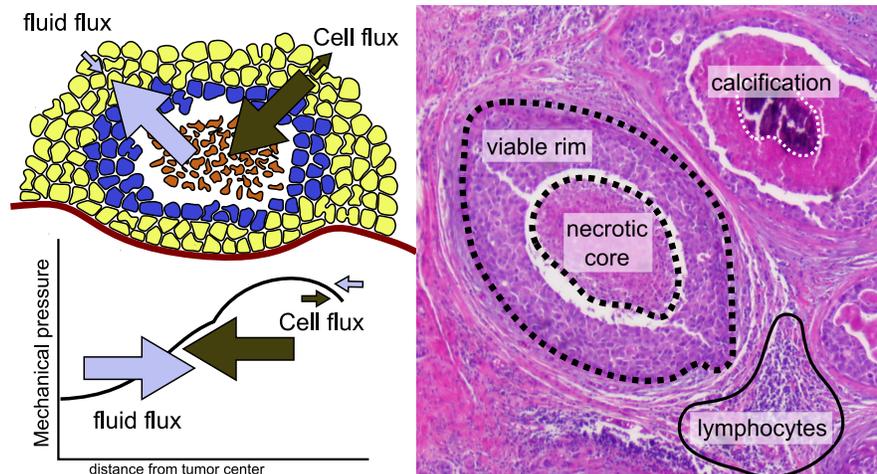
Fig. 1 Left: Proliferation in the viable rim (yellow cells) generates a cell flux (dark gray arrows) that can balance with fluid flux (pale blue arrows) created by lysing cells in the necrotic core (brown cell debris), resulting in steady tumor sizes. Adapted with permission from [52]. **Right:** Typical ductal carcinoma in situ (DCIS) duct cross-sections showing the outer viable rim, inner necrotic core, calcifications, and an inflammatory response. Adapted from [56] with permission.
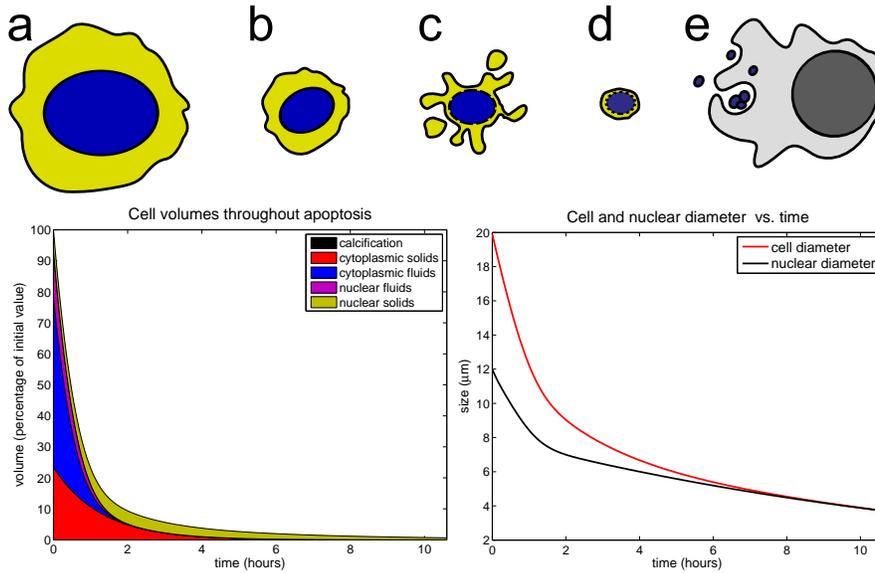
Fig. 2 Apoptosis schematic. Top: (a-b) While pro-apoptotic signals work to activate initiator cas-pases and then effector caspases to degrade subcellular structures and DNA, the cell rapidly shrinks by removing fluid. (c) The cell sheds its cytoplasm as membrane-encapsulated blebs. (d-e) Chro-matin is condensed. DNA is fragmented, encapsulated into apoptotic bodies, and phagocytosed by nearby cells. **Bottom:** Preliminary simulation [64] of apoptotic cell volume composition (left) and nuclear/total diameters (right). Figures provided courtesy of [64].

In the nucleus, the chromatin condenses and is henceforth degraded by en-dogeneous endonucleases into short fragments of DNA (Fig. 2(top:d)). Protein cross-linking (e.g., by transglutaminase [32]) helps to bundle these fragments into coherent, membrane-encapsulated *apoptotic bodies* [4, 25, 44, 46], which are fi-nally phagocytosed (ingested) and degraded by macrophages or other nearby cells [25, 44]. See Fig. 2(top:e). For more information on apoptosis, the reader is encour-aged to consult several excellent reviews (e.g., [25, 44, 46, 65, 87]).

2.1.1 Estimates of apoptosis time scales

In [55–57], Macklin et al. analyzed the experimental biology and clinical literature to estimate the main apoptosis time scales. The overall duration of apoptosis was estimated at 8-9 hours, with an approximately 2-hour lag until detectable cleaved Caspase-3 activity, and an additional hour of lag prior to detection by TUNEL assay. Mumenthaler et al. are now directly measuring these and other apoptosis time scales with *in vitro* experiments on MCF-7 and related breast cancer cell lines [68]. In preliminary results, we observed cell water loss to be very fast: most water is lost within the first hour of apoptosis. We also observed that the cytoplasm blebbs and loses much of its volume within three hours, leaving a degrading nucleus for the remainder of apoptosis. These preliminary observations are consistent with other

experiments (e.g., [30, 88]), which estimated apoptosis to last 8-9 hours [30], and measured rapid 60% volume losses early in apoptosis [88].

2.2 Basic biology of necrosis and calcification

In contrast to apoptosis, necrosis is a relatively energy-independent process, spanning a variety of time and spatial scales [46, 66]. In the context of cancer biology, necrosis is most frequently the result of cellular energy depletion, rather than a "planned" event [6]. Thus, while apoptotic cells generally appear sporadically as isolated, shrunken cells, necrotic tumor cells are found in large contiguous regions (i.e., necrotic cores) where oxygen and glucose are too low to sustain cell survival [44, 87]. Necrosis also differs from apoptosis in that it triggers an inflammatory response, due to the dysregulated release of intracellular proteins into the microenvironment [6, 46]. Indeed, inflammatory responses can readily be seen in pathology images near necrotic tumors; see Fig. 1(right) for one such example.
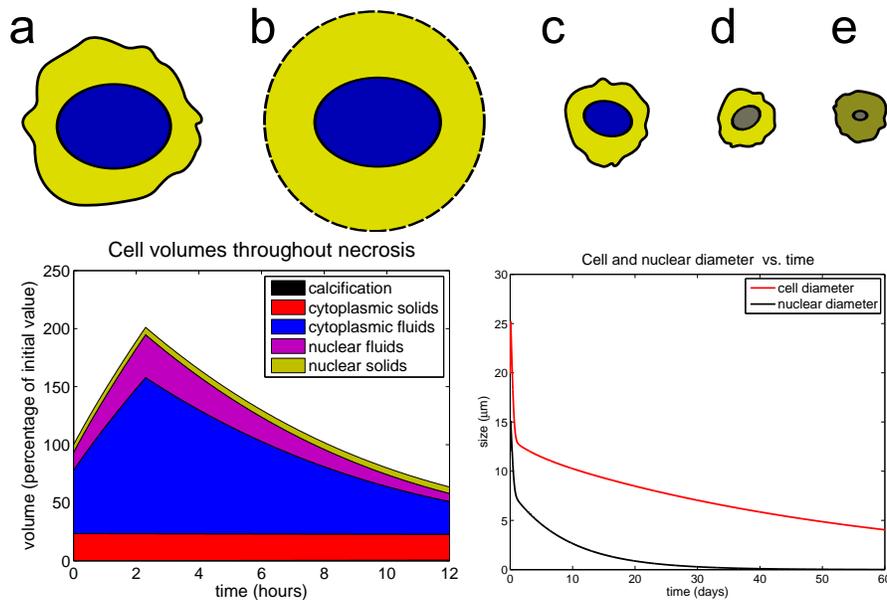

Fig. 3 Necrosis schematic. Top: (a-b) The necrotic cell swells until its membrane splits and leaks its fluid content (c). Its remaining nuclear solid content degrades (d), and the remaining cytoplasm degrades and is sometimes calcified (e). **Bottom:** Preliminary simulation [64] of early necrotic cell volume composition (left) and nuclear/total diameters (right). Figures courtesy of [64].

In the early stages of necrosis (more properly called *oncosis* [46, 65]), energy depletion causes the cell's ion pumps to shut down, resulting in rapid swelling by os-

mosis. This swelling has traditionally been a key feature differentiating necrotic/oncotic cell death from apoptotic cell death in pathology and *in vitro* biology [44, 46, 65]. The cell swells to several times its original volume, lyses (splits open), and slowly leaks fluids and other protein contents into the surrounding microenvironment [46]. See Fig. 3(top:a-c and bottom:left). Disintegrating lysosomes can release enzymes that help to further degrade the cell [6]. As in apoptosis, the nucleus displays some (irregular) chromatin condensation and shrinkage (pyknosis). However, the DNA is not cleaved into regularly-sized fragments, nor is it encapsulated into apoptotic bodies. Instead, it remains and degrades over time, eventually rupturing and dissipating into the remaining cytoplasm. See Fig. 3(top:d and bottom:right). In many tumors, necrotic tissue is removed by infiltrating macrophages; see the mathematical modeling of this process (and corresponding references) in [73]. We note that this brief overview of early-to-mid necrosis is a simplification, and the lines between apoptosis and necrosis can be blurred. For example, apoptotic bodies that are not cleared can become necrotic [44, 65], and while necrosis is seemingly "passive", it involves numerous significant biochemical processes [7, 46]. Excellent reviews of necrosis can be found in [6, 7, 46, 66, 87].

Fig. 4 Cell volume composition during later necrosis: Viewed on the long time scale of necrosis and calcification, early cell swelling and lysis are a fast perturbation on the longer-term trends of solid content calcification and degradation. Figure provided courtesy of [64].
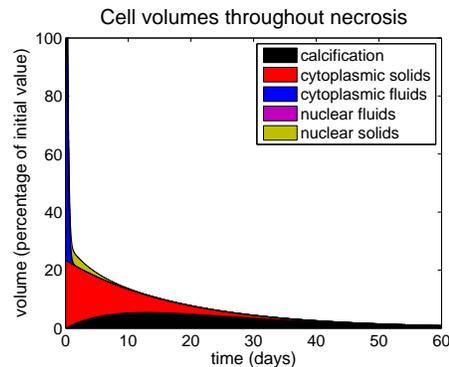
2.2.1 Dystrophic calcification

In DCIS, the necrotic core is separated from immune cells (and the stroma) by an intact basement membrane, preventing the removal of necrotic material. Instead, it remains and continues to degrade. In this and other cancers where the necrotic material is not cleared but rather persists for long periods of time, the necrotic core can undergo *dystrophic calcification* [40, 47]. In this process, calcium ions interact with remaining phospholipids in the necrotic cell (the membrane, vesicles, etc.) to nucleate and grow calcium phosphate crystals [47]. See Fig. 3(top:e), the example in Fig. 1(right), and Fig. 4. How this process transpires *in vivo* is still poorly understood.

2.2.2 Estimates of necrosis and calcification time scales

In [55–57], Macklin et al. estimated the various time scales of necrosis and calcification, many of which have not been experimentally measured for carcinoma. We estimated initial cell swelling and lysis to occur on the order of 2-6 hours. Based upon experimental reports on aortic calcification [34, 42, 48] and our previous computations [55–57], we estimate calcification to take on the order of 15-20 days [56]. Based upon our insights from [56] (See Section 4.3) and the existence of necrotic tissue with intense eosin staining (a sign of cytoplasm with significant water loss and little calcification) and compact, partly-degraded nuclei, we estimate that water loss occurs more quickly than pyknosis, and that pyknosis is a faster process than calcification. We have recently hypothesized and found good evidence that calcifications degrade at a very long time scale (on the order of two to three months) [56]. See Section 4.5. Thus, necrosis and calcification have processes that operate on time scales ranging from hours to months.

3 Early continuum modeling results: impact of necrotic core mechanics on tumor progression, morphology, and stability

Following earlier tumor growth models that included necrotic cores [12, 89, 90] and an earlier non-necrotic free boundary formulation of tumor growth [18], Macklin and Lowengrub developed a model of non-symmetric avascular tumor growth in heterogeneous tissues which included necrosis [51, 58–62]. We modeled the tumor as an incompressible fluid (with constant cell density) moving in a porous medium—the ECM. We used a sharp interface approach, where $\Omega(t)$ denoted the moving tumor volume with boundary $\Sigma(t)$; we denoted the surrounding host tissue by Ω_{H}. In [60], we set Ω_{H} to enclose Ω in an $L \approx 100 - 200 \,\mu\mathrm{m}$ ring of tissue:

$$\Omega \cup \Omega_{\mathrm{H}} = \left\{ \mathbf{x} : |\mathbf{x} - \mathbf{x}_{\mathrm{center}}(t)| \leq R(t) + L \right\}, \tag{1}$$

where

$$R(t) = \max \left\{ |\mathbf{x} - \mathbf{x}_{\mathrm{center}}(t)| , \mathbf{x} \in \Omega(t) \right\}, \tag{2}$$

and where $\mathbf{x}_{\mathrm{center}}$ is the center of mass of $\Omega(t)$. We scaled space by L (the nutrient diffusion length scale) and time by a mechanical relaxation time scale $\lambda_{\mathrm{R}}^{-1}$. The time is rescaled in all plots to correspond to the cell mitosis time scale $\lambda_{\mathrm{M}}^{-1} \approx 24$ hours. See [51, 58–60] for more details.

We introduced a single nondimensional "nutrient" σ which was required for cell survival and drove growth. The nutrient was released by the host vasculature at $\partial \left(\Omega \cup \Omega_{\mathrm{H}} \right)$, diffused through the non-vascularized nearby host tissue Ω_{H} to the tumor, and was then consumed by tumor cells in Ω. Following [18] and as described in [58], we make the quasi-steady assumption: nutrient transport and consumption occur on much faster time scales than cell proliferation and tissue deformation, and so on the time scale of simulation, $\partial \sigma / \partial t \approx 0$. Thus, σ satisfies

$$0 = \nabla \cdot (D_H \nabla \sigma) \qquad\qquad \mathbf{x} \in \Omega_H$$
$$0 = \nabla \cdot (D_T \nabla \sigma) - \sigma \qquad \mathbf{x} \in \Omega \qquad\qquad (3)$$

subject to boundary and matching conditions

$$[\sigma]_\Sigma = 0 \qquad\qquad [D \nabla \sigma \cdot \mathbf{n}]_\Sigma = 0$$
$$\sigma(\mathbf{x})\big|_{\partial(\Omega_H \cup \Omega)} = 1, \qquad\qquad (4)$$

where for any $\mathbf{x} \in \Sigma$, the jump function $[f(\mathbf{x})]_\Sigma$ is defined as

$$[f(\mathbf{x})]_\Sigma = \lim_{\Omega \ni \mathbf{y} \to \mathbf{x}} f(\mathbf{y}) - \lim_{\Omega_H \ni \mathbf{y} \to \mathbf{x}} f(\mathbf{y}). \qquad\qquad (5)$$

In [60], $D_T = 1$ as a result of nondimensionalization. The nutrient is used to implicitly define viable and necrotic regions (Ω_V and Ω_N, respectively) of the tumor:

$$\Omega_V = \{\mathbf{x} \in \Omega \text{ such that } \sigma(\mathbf{x}) \geq \sigma_N\}$$
$$\Omega_N = \{\mathbf{x} \in \Omega \text{ such that } \sigma(\mathbf{x}) < \sigma_N\}, \qquad\qquad (6)$$

where σ_N is the necrotic threshold value of σ. Note that $\Omega = \Omega_V \cup \Omega_N$.

Within the tumor's viable rim, cells were assumed to proliferate at a rate proportional to σ and apoptose at a constant background rate. In Ω_N, the model degraded necrotic debris and released volume, acting as a biomechanical stress relief. We assumed the host tissue was in homeostasis (proliferation and apoptosis were in balance), but cells and tissue could be displaced by forces generated by the tumor. The tissue moved with velocity $\mathbf{u}$ in response to forces generated by cell proliferation and death. Under the incompressibility and constant cell density assumptions, the local rate of volume change is given by $\nabla \cdot \mathbf{u}$. In dimensionless form,

$$\nabla \cdot \mathbf{u} = \quad 0 \qquad\qquad \mathbf{x} \in \Omega_H$$
$$\nabla \cdot \mathbf{u} = \quad G(\sigma - A) \qquad \mathbf{x} \in \Omega_V \qquad\qquad (7)$$
$$\nabla \cdot \mathbf{u} = -G\, G_N \qquad\qquad \mathbf{x} \in \Omega_N,$$

where G, A, and G_N are dimensionless parameters characterizing the rates of cell proliferation, apoptosis, and necrotic tissue volume loss relative to the time scale λ_R^{-1}. See [60] for greater detail on the nondimensionalization and these parameters.

We introduced a dimensionless proliferation-generated mechanical pressure p as a simplified model of tissue stress, and assumed a Darcy flow response: cells can respond to the pressure by overcoming cell-cell and cell-ECM adhesion and moving through the porous medium (the ECM) supporting the cells. Moreover, the ECM itself can deform in response to p. Hence, $\mathbf{u} = -\mu \nabla p$, where μ is the tissue mobility (its ability to respond to pressure gradients). Assuming constant cell-cell adhesive forces and cell density throughout Ω_V, cell-cell adhesion can be modeled as a surface tension proportional to the curvature κ along $\Sigma(t)$. Thus, as in [18],

$$-\nabla \cdot (\mu_H \nabla p) = 0 \qquad\qquad\qquad \mathbf{x} \in \Omega_H$$
$$-\nabla \cdot (\mu_T \nabla p) = \begin{cases} G(\sigma - A) & \mathbf{x} \in \Omega_V \\ -G G_N & \mathbf{x} \in \Omega_N \end{cases} \qquad (8)$$

subject to boundary and matching conditions

$$[p]_\Sigma = \kappa \qquad [\mu\nabla p \cdot \mathbf{n}]_\Sigma = 0$$
$$p(\mathbf{x})\big|_{\partial(\Omega_{\mathrm{H}}\cup\Omega)} = 0. \tag{9}$$

In [60], $\mu_{\mathrm{T}} = 1$ as result of nondimensionalization.

We implicitly tracked the moving boundary position using the level set method: an auxiliary distance function ϕ satisfies $\phi < 0$ in Ω, and $\phi > 0$ in Ω_{H}, $\phi = 0$ on Σ, the outward normal vector is given by $\mathbf{n} = \nabla\phi$, and $\kappa = \nabla\cdot\mathbf{n}$. The outward normal velocity of $\Sigma(t)$ is obtained by evaluating $\mathbf{u}\cdot\mathbf{n} = -\lim_{\Omega\ni\mathbf{y}\to\mathbf{x}}\mu_{\mathrm{T}}\nabla p(\mathbf{y})\cdot\mathbf{n}$ for any $\mathbf{x} \in \Sigma$. The motion of Σ then becomes an advection equation for ϕ [51, 58–62]. We solved Eqns. (3-4) and (8-9) using a second-order accurate ghost fluid method [51, 58–62]. We let $D = D_{\mathrm{H}}/D_{\mathrm{T}}$ and $\mu = \mu_{\mathrm{H}}/\mu_{\mathrm{T}}$ denote the relative oxygenation and mechanical compliance of the surrounding host tissue, respectively.

### 3.1 Impact of necrotic core biomechanics: key results

As in earlier tumor spheroid models [12, 89, 90] and early non-symmetric necrotic tumor simulations in [93], our theoretical and numerical analyses [51] showed that even with $A = 0$, volume creation in the proliferative rim could balance with volume loss in the necrotic core, leading tumor spheroids to grow to a steady size. Our work had an additional insight: even during growth (and overall morphological instability), tumor proliferation and necrotic volume loss could equilibrate *locally*, leading to (1) a near-constant necrotic volume fraction, and (2) the emergence of characteristic feature sizes and shapes. For example, a tumor growing into well-perfused ($D > 1$), mechanically-stiff ($\mu \leq 1$) tissue develops invasive fingers with a characteristic width. See Fig. 5(left) for such an example.

The qualitative tumor behavior (classified as fragmenting, fingering, or hollow/compact growth) was primarily dependent upon the microenvironmental parameters D and μ. However, the quantitative behavior—viable rim thickness, necrotic volume fraction, overall growth rate, etc.—was strongly dependent upon tumor cell characteristics, particularly the necrosis parameters σ_{N} and G_{N}. The viable rim size was determined by the balance of nutrient penetration into the host tissue (D), apoptosis (A), and the tumor cells' resistance to hypoxia (σ_{N}). The size of the necrotic core was primarily determined by the rate of volume loss in necrotic tissue (G_{N}). See Fig. 5(right), where we show how the tumor varied with G_{N} for several values of G. A key finding was that while moderate rates of necrotic volume loss indeed contribute to the emergence of a steady state size for the spherical case, *fast* necrotic volume loss (large G_{N}) can destabilize the tumor morphology.

This work revealed a few outstanding problems with continuum necrosis models of the time. First, defining the necrotic region implicitly through σ as in Eqn. 6 could cause unexpected behavior for complex tumor morphologies. Particularly unstable tumors could experience frequent connection and disconnection of invasive
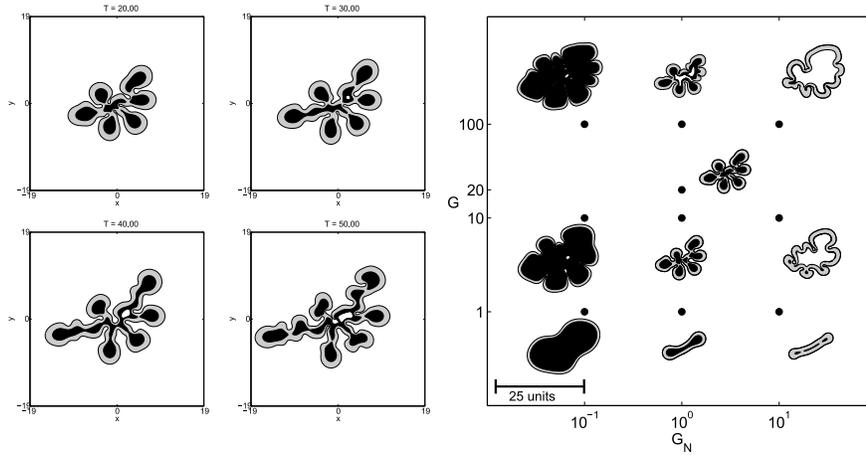
Fig. 5 Left: Growth of a necrotic avascular tumor into well-perfused, mechanically-stiff tissue. The invasive "fingers" and necrotic regions acquire relatively fixed, characteristic sizes.
Right: Impact of the rate of cell proliferation (G) and necrotic volume loss (G_N) on invasive fingering growth. G acts primarily as a time scale (tumor morphologies are the same but evolve more quickly with increased G), whereas larger values of G_N can destabilize the morphology (seen here as changing rounded protrusions into invasive fingers). **Legend:** Viable (gray) and necrotic tissue (black) grow in host tissue (white). Figures adapted with permission from [60].
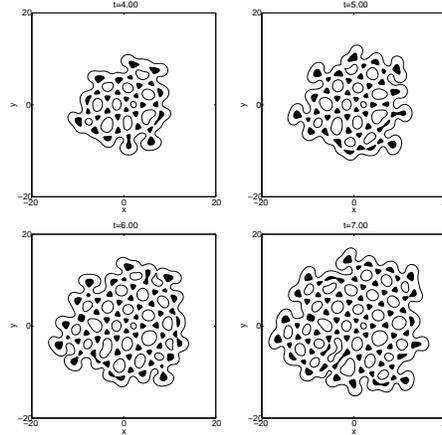
Fig. 6 A simulation of repeated encapsulation of host tissue by a growing tumor [58]. **Legend:** <u>White:</u> viable tumor. <u>Black:</u> necrotic tumor. Figure adapted with permission from [58].

fingers or bulbs [51, 58, 60]. (See Fig. 6 for an example of repeated encapsulation of host tissue.) Connectio or reconnection of invasive fingers or bulbs lead to rapid depletion of nutrient in the newly encapsulated host and tumor tissue, leading to a jump in necrosis. Subsequent disconnection would rapidly reperfuse the encapsulated regions, leading to the condition where $\sigma > \sigma_N$ in previously necrotic tissue. This necrotic tissue would "come back to life"—an impossibility. We solved these problems by introducing an additional level set function ϕ_N to separately track the necrotic core boundary [61, 62].

Second, because the continuum model linked together many biophysical effects into very few parameters (much to the benefit of mathematical analysis!), it was difficult to directly calibrate the model to experimental measurements. Model calibration required force-fitting the parameters to match experimental growth rate measurements, and then tuning the remaining parameters to match the simulated morphologies (as informed by parameter space investigations) to clinical or other observations (e.g., as in [33]). While this makes data-driven simulations possible, it can hinder the acceptance of mathematical modeling in the biological and clinical communities, who are concerned that complex models with too many free parameters can be tuned to any desired behavior without necessarily being biologically correct. Upscaling mechanistic cell-scale models can solve such problems, as in [23].

Lastly, even if the necrotic biomechanical properties can be rigorously estimated, continuum models like this one would need further refinement to incorporate both the slow and fast dynamics known to play a role in necrosis. In the next section, we will next describe a mechanistic, patient-calibrated agent-based model developed by Macklin and collaborators in [56] to examine these and other issues.

4 Recent agent-based modeling results: impact of necrotic core biomechanics on DCIS

Agent-based modeling affords us the opportunity to examine the multiscalarity of necrosis and calcification by implementing both fast and slow time scale processes in individual cells and investigating the emergent whole-tumor biomechanics and clinical progression. We present recent work by Macklin et al. in simulating DCIS for individual patients [54–57]. The work discussed below includes the most detailed model of cell necrosis to date, and the first model of calcification. It also includes the first patient-specific calibration method to use clinically-accessible pathology from a single time point, as might be available in a standard biopsy.

4.1 Model overview

In [54–57], Macklin et al. developed a patient-calibrated, lattice-free agent-based cell model and applied it to DCIS. Each virtual cell (an agent) has a position $\mathbf{x}$, velocity $\mathbf{v}$, and time-dependent physical properties. In particular, each cell has a volume $V(t)$ and nuclear volume $V_N(t)$, which can readily be expressed as equivalent spherical cell and nuclear radii $R(t)$ and $R_N(t)$, respectively. The cell also has a maximum adhesion interaction distance $R_A > R(t)$, which models both the cell's deformability and uncertainty in its morphology [56]. See Fig. 7(left).

The cell's velocity (and hence position) is governed by the balance of forces acting upon it: cell-cell adhesion ($\mathbf{F}_{cca}$) and "repulsion" (resistance to deformation: $\mathbf{F}_{ccr}$), cell-BM adhesion and repulsion ($\mathbf{F}_{cba}$ and $\mathbf{F}_{cbr}$), fluid drag ($-\nu\mathbf{v}$), cell-ECM
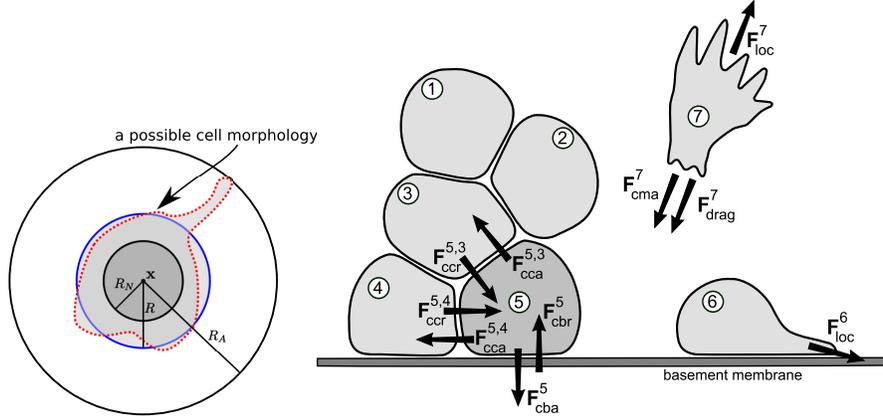
Fig. 7 Left: Cell position $\mathbf{x}$, maximum adhesion interaction distance R_A, volume V (light gray area), nuclear volume V_N (dark gray area), and equivalent radii R and R_N.
Right: Key forces in the model, labeled for cell 5. Figures reprinted with permission from [56].

adhesion ($\mathbf{F}_{cma} = -c_{cma}E$, where E is the local ECM density), and the net locomotive (motile) force $\mathbf{F}_{loc}$. These forces are balanced by Newton's second law (conservation of linear momentum). As in [22, 35, 75], we use the "inertialess" assumption of fast force equilibration to explicitly express the velocity of cell i:

$$\mathbf{v}_i = \frac{1}{\underbrace{\nu + c_{cma}^i E}_{\text{cell-medium interactions}}} \left(\overbrace{\sum_{\substack{j=1 \\ j \neq i}}^{N(t)} \left(\mathbf{F}_{cca}^{ij} + \mathbf{F}_{ccr}^{ij} \right)}^{\text{cell-cell interactions}} + \overbrace{\mathbf{F}_{cba}^i + \mathbf{F}_{cbr}^i}^{\text{cell-BM interactions}} + \mathbf{F}_{loc}^i \right), \quad (10)$$

where $N(t)$ is the number of simulated cells/agents at time t. For this discussion, we set $E \equiv 0$ and $\mathbf{F}_{loc} = \mathbf{0}$ to model nonmotile cells contained in a lumen without ECM. See [56] for the specific forms of the forces, which were modeled using potential functions with finite interaction distances, consistent with the maximum adhesion interaction distance R_A. These forces are labeled for Cell 5 in Fig. 7(right).

Each cell has a phenotypic state $\mathcal{S}(t) \in \{\mathcal{A}, \mathcal{P}, \mathcal{Q}, \mathcal{N}\}$, where $\mathcal{A}$ cells are apoptosing, $\mathcal{P}$ cells are proliferating (in non-G_0), $\mathcal{Q}$ cells are quiescent (in G_0), and $\mathcal{N}$ cells are necrotic. Transitions between phenotypic states are governed by microenvironment- and signaling-dependent stochastic processes. For example, quiescent cells enter the cell cycle with a (nondimensionalized) O_2-dependent probability:

$$\text{Prob}\left(\mathcal{S}(t+\Delta t) = \mathcal{P} | \mathcal{S}(t) = \mathcal{Q}\right) = 1 - \exp\left(-\int_t^{t+\Delta t} \overline{\alpha}_{QP} \frac{O_2(s) - O_{2,\text{hypoxic}}}{1 - O_{2,\text{hypoxic}}} \, ds\right)$$

$$\approx \overline{\alpha}_{QP} \left(\frac{O_2(t) - O_{2,\text{hypoxic}}}{1 - O_{2,\text{hypoxic}}}\right) \Delta t, \quad (11)$$

where $\overline{\alpha}_{QP}$ is the normoxic $\mathcal{Q} \to \mathcal{P}$ transition rate (when $O_2 = 1$), and $O_{2,\text{hypoxic}}$ is the hypoxic oxygen threshold. The $\mathcal{Q} \to \mathcal{A}$ transition is similar but does not depend upon O_2. Cells become irreversibly necrotic ($\mathcal{S} = \mathcal{N}$) when $O_2 < O_{2,\text{hypoxia}}$. The proliferative and apoptotic states have fixed durations τ_P and τ_A. Cell volume and other key properties are controlled by a "sub-model" for each phenotypic state. Proliferating cells in $\mathcal{P}$ divide in half after progressing through S, G_2, and M; their two daughters spend G_1 growing (linearly) to their mature volumes and then return to $\mathcal{Q}$. Apoptotic cells are removed from the simulation after τ_A. We do not impose contact inhibition (a common feature for cellular automata models: reduced $\mathcal{Q} \to \mathcal{P}$ transitions for cells when surrounded by neighbor cells); this is because patient pathology for Ki-67 (a proliferation marker) frequently shows proliferating cells that are completely surrounded by other cells. As we shall see, a properly-calibrated mechanistic model can predict quantitatively-reasonable DCIS growth without need for contact inhibition. See [56] for full details on the proliferative and apoptotic sub-models.

4.1.1 Necrosis sub-model

Let τ denote the elapsed time spent in the necrotic state. Define τ_{NL} to be the length of time for the cell to swell, lyse, and lose its water content, τ_{NS} the time for all surface receptors to become functionally inactive, and τ_{C}, the time for calcification to occur. We assume that $\tau_{\text{NL}} < \tau_{\text{NS}} < \tau_{\text{C}}$.

We assume a constant rate of calcification, reaching a radiologically-detectable level at $\tau = \tau_{\text{C}}$. If C is the nondimensional degree of calcification (scaled by the detection threshold), then $C(\tau) = \tau / \tau_{\text{C}}$ for $0 \leq \tau \leq \tau_{\text{C}}$, and $C(\tau) = 1$ otherwise. (We do not track further calcification after τ_{C}.) We model the degradation of any surface receptor S (scaled by the non-necrotic expression level) by exponential decay with rate constant $\log 100 / \tau_{\text{NS}}$, so that $S(\tau_{\text{NS}}) = 0.01 S(0)$. We set $S(\tau) = 0$ for $\tau > \tau_{\text{NS}}$.

To model the necrotic cell's volume change, let f_{NS} be the maximum percentage increase in the cell's volume (just prior to lysis), and let V_0 be the cell's volume at the onset of necrosis. Then we model:

$$V(\tau) = \begin{cases} V_0 \left(1 + f_{\text{NS}} \frac{\tau}{\tau_{\text{NL}}}\right) & \text{if } 0 \leq \tau < \tau_{\text{NL}} \\ V_{\text{N}} & \text{if } \tau_{\text{NL}} < \tau. \end{cases} \tag{12}$$

To model uncertainty in the cell morphology during lysis, we randomly perturb its location $\mathbf{x}$ such that its new radius $R(\tau_{\text{NL}})$ is contained within its swelled radius $R(0) \left(1 + f_{\text{NS}}\right)^{\frac{1}{3}}$.

4.1.2 Other model details and numerical implementation

As we described in [56], microenvironmental quantities are modeled with reaction-diffusion equations throughout the computational domain. Uptake terms (e.g., for O_2) are created by a coarse-graining technique: first construct a high-resolution up-

take term that resolves each cell's volume, then average it across a lower-resolution mesh (mesh size $\sim 1/10$ the appropriate diffusion length scale) before solving the reaction-diffusion equation. We apply Dirichlet conditions on the BM, and use Neumann conditions wherever the lumen intersects the computational boundary.

We represent the basement membrane using a signed distance function d satisfying $d > 0$ in the lumen, $d < 0$ in the stroma, $d = 0$ on the basement membrane, and $|\nabla d| \equiv 1$. We introduce an auxiliary data structure to reduce the overall computational cost from $\mathcal{O}\left(N(t)^2\right)$ to $\mathcal{O}\left(N(t)\right)$, where $N(t)$ is the number of simulation objects at time t [56]. We implemented the model in cross-platform, object-oriented C++; we currently plan to open source the simulation framework in the next year. Towards that end, we introduced MultiCellXML, a new XML-based standard for sharing multicell agent simulation data. The supplementary material for [56] include sample DCIS simulation datasets (in MultiCellXML 1.0 format) and open source postprocessing and visualization code. See http://MathCancer.org/JTB_DCIS_2012/.

4.1.3 Calibration to individual patients, and key necrosis parameter values

In [56], we introduced the first calibration method to use individual patient pathology from a single time point, based upon processing several DCIS-affected ducts for the patient, as described in [23]. The proliferative index (PI: the percentage of Ki-67 positive cells in the viable rim) and apoptotic index (AI: the percentage of cleaved Caspase-3 positive cells in the viable rim) were combined with estimates of the proliferative time scale ($\tau_P = 18$ hours) and apoptotic time scale ($\tau_A = 8.6$ hours) and a population dynamic argument to calibrate the $\mathcal{A} \leftarrow \mathcal{Q} \leftrightarrow \mathcal{P}$ phenotypic transitions in the model. The cell density and experimental reports on cell mechanical response to deformation (see the references in [56]) were used to calibrate the mechanical parameters of the model. We calibrated oxygen transport by solving steady-state reaction-diffusion equations in a simplified cylindrical duct geometry and matching to the patient's measured viable rim thickness. In [56], we applied the calibration to a single anonymized DCIS patient with high-grade solid-type DCIS with comedonecrosis; we show the simulation (in a 1.5 mm, 2-D longitudinal section of duct) after 45 days of growth in this patient in Fig. 8. We recently combined this calibration method with an upscaling/coarse-graining argument to derive patient-specific predictions of surgical excision volumes in [23].

4.2 DCIS growth is linear; mammography and pathology sizes are linearly correlated; origins in necrotic cell water loss

In [56], we post-processed the simulation in one-hour increments to determine the mean proliferative index, apoptotic index, viable rim thickness, and density as functions of time, as well as the farthest viable cell position ($x_V(t)$: the virtual pathology size) and the farthest calcified cell position ($x_C(t)$: the virtual mammography size).
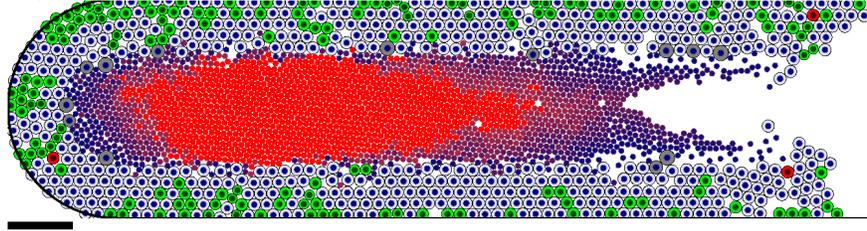
Fig. 8 Patient-calibrated DCIS simulation: After calibrating to a patient's pathology data as described in [56], we simulate 45 days of DCIS growth. **Legend:** *Viable rim:* The black curve denotes the basement membrane. The small blue circles are cell nuclei, quiescent cells ($\mathcal{Q}$) are pale blue, proliferating cells ($\mathcal{P}$) are green, and apoptosing cells ($\mathcal{A}$) are red. *Necrotic core:* Necrotic cells ($\mathcal{N}$) are grey until they lyse; their solid fraction remains as debris (dark circles in center of duct). The shade of red indicates the level of calcification; bright red debris are clinically-detectable microcalcifications ($\mathcal{N}$ with $t > \tau_C$). **Bar:** 100 μm. Adapted with permission from [56].

Open source C++ postprocessing code is given at MathCancer.org. We plot x_V (solid blue curve) and x_C (dashed red curve) in Fig. 9(left). After early transient dynamics, a linear (constant-rate) growth pattern emerges. The tumor advances at approximately 10.2 mm/year (obtained by the linear least-squares fit of x_V), whereas the calcification grows at 9.15 mm/year (linear least-squares fit of x_C). Due to these linear growth rates, the tumor's mammography and pathology sizes were predicted to be linearly correlated, with a linear least-squares correlation:

$$\text{pathology size} \approx 0.4203 \text{ mm} + 1.117 \text{ mammography size}, \tag{13}$$

where all measurements are in mm. See the blue points in Fig. 9(right).
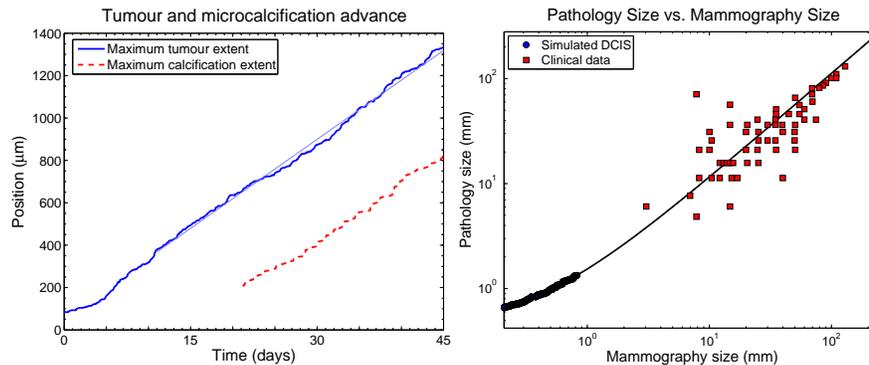
Fig. 9 Left: Over long times, the DCIS advances linearly at approximately 1 cm/year (top curve); the calcification also grows linearly. **Right:** The simulation (blue circles) predicts a linear correlation between the DCIS mammography and pathology sizes. When extrapolated over two orders of magnitude, the predicted correlation shows good agreement with clinical reports (red squares). Figures reproduced with permission from [56].

These predictions are qualitatively and quantitatively consistent with clinical estimates of DCIS growth. Linear DCIS growth has been reported in a clinical study correlating changes in mammographic size with time between mammograms [15]. Another clinical study on microcalcifications reported that high-grade DCIS grows at 7.1 mm per year (along an axis to the nipple) [86]. They also analyzed the data in [15], deriving 13 mm/year and 6.8 mm/year mean and median growth rates, respectively. According to our relationship in Eqn. 13, these correspond to pathology growth rates on the order of 7.6 to 14.5 mm/year. Hence, both our mammography and pathology growth rate predictions are quantitatively consistent with the clinical literature. [78] compared the maximum calcification diameter in mammograms (corresponds to x_C) with the measured pathologic tumor size (corresponds to x_V) in 87 patients, finding a significant linear correlation between these measurements. When we extrapolate our linear relationship in Eqn. 13 over two orders of magnitude (from the 1 mm scale to the 1cm and 10 cm scales, approximating 1 to 10 years of growth), our extrapolated mammography-pathology correlation (the curve) shows an excellent quantitative agreement with these 87 data points (red squares) in Fig. 9(right). This is a surprising and interesting result, which suggests that absent major alterations in signaling or microenvironmental factors, a patient's long-time growth dynamics may be established very early in progression.

These clinical phenomena can be understood as emergent from the underlying biophysics of the viable rim and necrotic core. Due to oxygen transport limitations, cell proliferation is confined to an approximately 80 μm viable rim. As the tumor grows, a steady pattern of flux emerges: proliferating cells towards the tumor leading edge are directed primarily towards empty space ahead of the tumor. Farther back, it is more mechanically favorable for mitosing cells to push their neighbors towards the duct center (against fewer cells) than along the duct (against more cells). Viable cells get pushed into hypoxic regions of the lumen, where they become necrotic and accumulate to fill the duct. This results in a linear growth pattern, as forward-directed proliferative cell flux is constrained to the leading edge of the tumor.

Necrotic cell lysis sustains this process. Whenever a necrotic cell lyses, its former volume is converted to a small core of cellular debris and a large pocket of (released) fluid, which is easily occupied by other cells. Thus, the earlier flux dynamic is maintained: proliferating cells on the outer edge of the duct push interior cells towards the necrotic core, diverting much of the overall cell flux inwards rather than towards the tumor leading edge. Hence, necrotic cell lysis acts as a mechanical stress relief, analogously to the mechanical pressure sink terms used in [58–61].

This can be further confirmed by altering the necrosis model. In [55, 57], we used a more gradual model of necrotic cell volume loss, where fluid "leakage" was spread over $\tau_C = 15$ days. The tumor advance accelerated as the viable rim grew, consistent with exponential growth. In those simulations, the rate of biomechanical stress relief in the necrotic core was too slow, causing more of the proliferative cell flux to be directed along the duct, preventing sustained linear growth. When we set $\tau_{NL} = \tau_C = 15$ days, we observed accelerating, exponential-like growth (blue curve after initial transient dynamics) [56]. See Fig. 10(left). Generally, we found that all simulations exhibited exponential-like growth for approximately τ_{NL} time

after the first instance of necrosis. For sufficiently small τ_{NL} (under 1 day), the brief exponential growth phase could not be detected. This mechanism suggested to us that because the lumen/necrotic core acts as a "reservoir" of mechanical stress relief to absorb proliferative cell flux, DCIS growth should be fastest in small ducts, and slowest in larger ducts. In simulations, we found this to be supported [56]. See Fig. 10(right). We found an inverse relationship between duct radius R_{duct} and the DCIS growth rate x'_V (the red curve in Fig. 10(right)):

$$x'_V \approx 20.52 + e^{6.085 - 0.02584 R_{duct}} \, \mu\text{m/day}. \tag{14}$$

Notice that as $R_{duct} \to \infty$, we find a minimum growth rate of 7.5 mm/year, or a mammography growth rate (by Eqn. 13) of 6.7 mm/year. Cases with slower growth would need to be attributed to reduced oxygen or altered cell signaling.
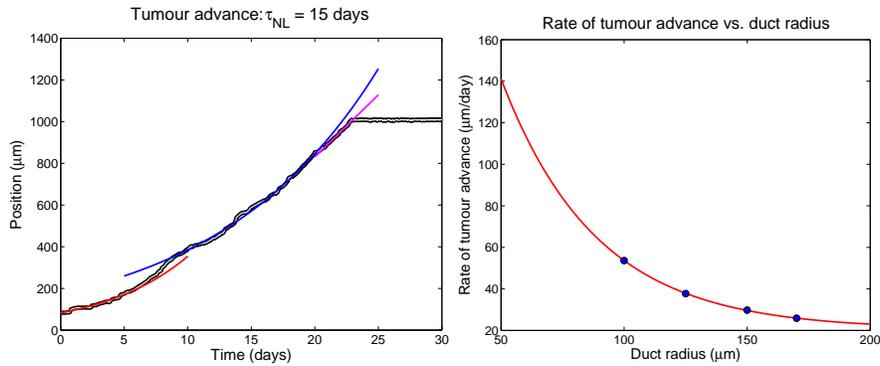

Fig. 10 Left: Delaying cell lysis leads to a completely filled necrotic core, which redirects proliferative cell flux along the duct. This results in exponential-like growth (blue curve). **Right:** Larger ducts have a greater "reservoir" available to absorb proliferative cell flux through necrotic cell lysis, leading to slower growth than in smaller ducts. Figures reproduced from [56] with permission.

4.3 Proliferative cell flux and multiscale necrosis lead to a stratified, age-structured necrotic core

Thus far, we have focused upon the gross macroscopic behavior of DCIS: the emergent growth rate and the relationship between mammography and pathology. We now turn our attention to the finer microstructure of the tumor. In Fig. 11(top), we highlight several characteristic cross-sections of our DCIS simulation at 45 days.

In **Slice a**, there is a viable rim of thickness comparable to the remainder of the tumor, but with little visible evidence of necrosis. Biologically, this section of the tumor is no different than portions with necrosis (i.e., hypoxia is significant). This raises the possibility that in cases where too few ducts are sampled, a pathologist
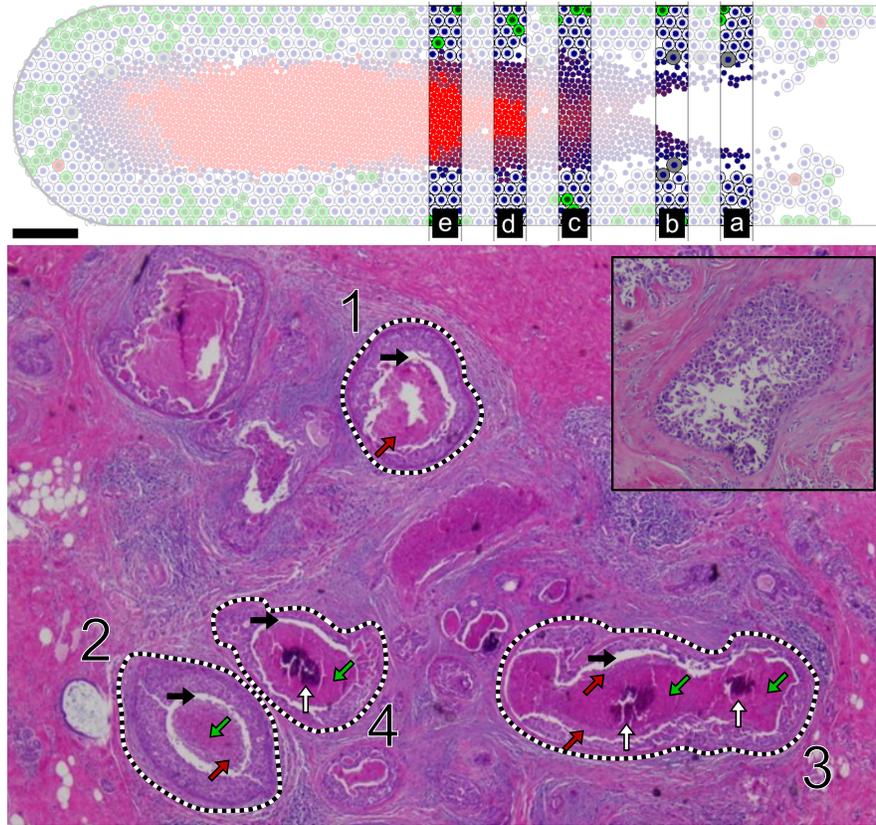
Fig. 11 Top: Patient-calibrated DCIS simulation from Fig. 8, with selected cross-sections highlighted to emphasize the emergent necrotic core microstructure. Near the leading edge (slice a), little necrotic debris has accumulated in the lumen. Farther back, relatively intact necrotic debris forms a ring near the necrotic boundary (slice b). Farther still, the lumen is completely filled with necrotic debris, with increasing degradation towards the center (slice c). Farther back, the oldest material is calcified, surrounded by relatively degraded debris (slice d). Calcification increases with distance from the leading edge (slice e). Reproduced with permission from [56].
Bottom: All the predicted necrotic core microstructures are observed in the patient's hematoxylin and eosin (H&E) pathology. Red arrows (pointing up and right) show necrotic debris with relatively intact nuclei. Green arrows (pointing down and left) show relatively degraded necrotic debris. White vertical arrows show calcification. Black arrows show the mechanical tear at the perinecrotic boundary. Simulated slice b predicts the microstructure seen in duct 1. Simulated slice c corresponds to duct 2. Simulated slice d corresponds to duct 3. Simulated slice 3 corresponds to duct 4. **Inset:** A duct similar to slice a. Pathology images adapted with permission from [56].

may fail to observe comedonecrosis, potentially (and incorrectly) changing the patient's Van Nuys Prognostic Index score [84] and affecting treatment decisions. This could be particularly true in cases where $\langle PI \rangle / \tau_P \approx \langle AI \rangle / \tau_A$, as little net cell flux from the viable rim to the necrotic core would be expected [56].

Farther from the tumor leading edge in **Slice b**, a ring of necrotic debris surrounds a hollow duct lumen. In cross sections like this, there has not yet been sufficient tu-

mor cell flux from the viable rim to completely fill the lumen with necrotic debris. Farther still from the leading edge in **Slice c**, there has been sufficient cell flux to fill the lumen with necrotic material; an outermost band of intact necrotic nuclei encircles a central region of mostly degraded nuclei (modeled here simply as partly calcified). Farther from the leading edge in **Slice d**, a thin outermost band of relatively intact necrotic nuclei surrounds an inner band of mostly degraded necrotic material and an inner core of microcalcification. In **Slice e**, the microcalcification is larger, and the outermost band of intact necrotic nuclei is largely gone. The necrotic core is increasingly calcified with distance from the tumor leading edge.

Overall, the model predicts an age-ordered necrotic core microstructure, with oldest material in the center surrounded by increasingly newer, less-degraded, and less-calcified material. Indeed, all these cross-sections can be found in our patient. See the hematoxylin and eosin (H&E) stained section in Fig. 11(bottom). Slice b corresponds to **Duct 1**, where a ring of relatively intact necrotic debris (red arrows) surrounds an as-yet unfilled lumen. Slice c corresponds to **Duct 2**, where the entire lumen has been filled necrotic debris, which is more intact at its outer edge (red arrow), and increasingly degraded in its center (green arrow). Slice d corresponds to **Duct 3**, where a thinner ring of mostly intact nuclei (red arrows) surrounds an intermediate layer of mostly degraded debris (green arrows) and a central core of microcalcifications (white arrows). (Note that Duct 3 is likely the intersection of two or more ducts near a branch point.) Slice e corresponds to **Duct 4**, where a ring of degraded necrotic debris (green arrow) surrounds a larger calcification (white arrow). The **inset** shows a different duct from the patient that is similar to slice a.

This stratified structure arises from the overall flux of cells from the viable rim into the necrotic core, working in concert with the multiple time scales during necrosis. If any of these scales were changed or removed, the microstructure would be altered. Indeed, better accounting for the time scales of nuclear degradation and fluid loss would likely improve the quantitative match to the patient pathology [56, 64].

4.4 Fast time scale necrotic cell lysis and volume loss are responsible for mechanical "tears" at perinecrotic boundary

One notable feature of nearly every DCIS pathology section is a "tear" at the perinecrotic boundary. See the black arrows in Fig. 11(bottom). The conventional wisdom is that these tears are not actually present *in vivo*, but are instead artifacts that arise from tissue dehydration during sample preparation.

In [57], we implemented a preliminary necrosis sub-model where fluid volume was lost through the membrane gradually throughout necrosis, at a rate proportional to surface area and the remaining fluid fraction:

$$\frac{dV}{d\tau} = -\left(\frac{2}{\tau_N}\log 100\right)\left(4\pi R^2\right)\left(\frac{V - V_S}{V}\right), \tag{15}$$

Fig. 12 Early DCIS simulations [57] neglected fast necrotic cell swelling and implemented a gradual volume loss over 15 days. The simulations could not reproduce the tear at the perinecrotic boundary. Necrotic cell lysis was too slow to sustain linear growth. Adapted with permission from [57].
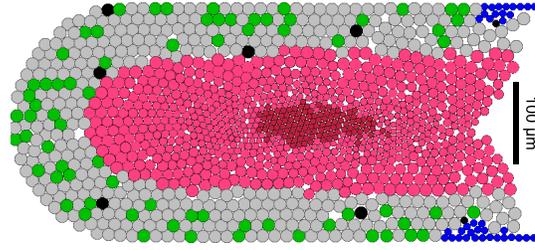

where $0 < \tau < \tau_C = \tau_N$ is the elapsed time since entering the necrotic state, V_S is the cell's solid fraction, and the coefficient was chosen to make this nonlinear ODE satisfy $V(\tau_N) \approx V_S$. Fast cell swelling and lysis were neglected. The simulation, plotted at 30 days in Fig. 12, did not predict a tear at the perinecrotic boundary. We therefore hypothesized that if the perinecrotic tear is not an artifact, it must be caused by a fast time scale process. In [56], based upon a more thorough review of necrosis biology (see Section 2.2), we implemented the current model with rapid necrotic cell swelling followed by rapid volume loss. These simulations did recapitulate the perinecrotic tear. See the tumor leading edge in Fig. 8.

The mechanistic model is based upon the balance of actual forces with biophysically sound parameter values, is calibrated to actual patient data, and successfully makes quantitative, validated predictions on DCIS progression. In light of this care we put into the biological and clinical accuracy of the model, we conclude that mechanical separation of the viable rim and necrotic core at the perinecrotic boundary, although exacerbated by tissue dehydration, is in fact a real phenomenon, rather than a simple artifact. Based upon this new insight, we now interpret tears and cracks in pathology sections as indicators of a tissue's local biomechanical strength.

4.5 Evidence of calcification degradation at a very long time scale

Our simulations (Fig. 8) predict a linear/casting-type calcification, where the calcification forms a long, solid "plug" in the center of the duct. See Fig. 13 for a mammographic image of casting-type microcalcifications. Other calcification morphologies (e.g., fine pleomorphic) are not predicted by the biophysical assumptions of our model. While casting-type calcifications correlate with comedonecrosis [85], they are only present in approximately 30-50% of DCIS [28,39]. Moreover, casting-type calcifications can be absent from small, high-grade DCIS, while present in larger, low-grade DCIS [28]. Additional biophysics (e.g., secretions, heterogeneous adhesion mechanics, or degradation over long time scales) are required to model the broader spectrum of observed calcifications in DCIS. Our H&E images (Fig. 11) support this idea. The central regions of many calcifications—which we have shown are associated with the "oldest" necrotic material—demonstrate significant cracks that suggest extensive degradation and weak cohesion.

Fig. 13 Mammogram of a
DCIS patient with character-
istic casting-type microcal-
cifications, labeled here with
red arrows. Image courtesy
of Andy Evans, University of
Dundee / NHS Tayside.
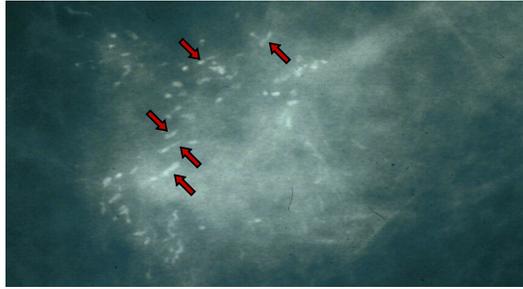
Phospholipids—such as those from subcellular structures that likely form a
"backbone" for the formation of microcalcifications—degrade with half-lives on
the order of 80 [3] to 300 hours [45] in non-pathologic tissue. Given this time scale,
we would expect necrotic tissues and their associated microcalcifications to degrade
over the course of a few months. This may partly explain rare cases of spontaneous
resolution of calcifications in mammograms, where calcifications become smaller
or occult without alternative explanations [81]: in slow-growing DCIS (e.g., with
both high PI and AI, as observed in high-grade DCIS [11]), calcifications may be
degraded more quickly than they are replaced by new necrotic material.

5 Discussion and looking forward

As we have seen, tissue necrosis and calcification are truly multiscale processes.
Early tissue-scale modeling [51, 58–62] (Section 3) provided key insights on the
role of tissue necrosis in steady tumor spheroid sizes, and its potentially destabiliz-
ing role when volume loss is rapid. Notably, these models can sufficiently predict
the impact of the necrotic core on the long-time volume and morphology of a tumor,
allowing quantitative predictions of progression. However, continuum modeling has
thus far focused on the slower time scale processes of fluid loss and solid degrada-
tion; reformulation would be required to incorporate fast time scale processes like
swelling and lysis. This is an interesting shortcoming, given that these are *key* fea-
tures used to differentiate necrosis (and oncosis) from apoptosis in pathology.

Models that consider the full spread of time scales in necrosis and calcification
can produce a rich spectrum of behaviors that match observations in pathology [55–
57] (Section 4). As hypothesized in [57] and investigated in [56], fast cell swelling
and lysis—so fundamentally characteristic of early necrosis—are responsible for the
tears ("artifacts") at the perinecrotic boundary that we consistently see in pathology.
From a continuum point of view, these are rapid perturbations that create persistent
and sharp discontinuities in the cell and necrotic debris distributions.

The simulated tumor microstructure—a viable rim (with greatest proliferation at
the outermost edge) surrounding a stratified, age-structured necrotic core—arises
from the multiscalarity of tissue necrosis and calcification. In the necrotic core,
the structure mirrors tissue age due to the steady flux from the viable rim into the

necrotic core: the newest, least degraded material surrounds increasingly degraded debris, with central calcifications in the oldest tissues [56]. All these features are consistently observed in patient pathology. Our work revealed a long-time deterioration of calcifications that may explain key features in mammography.

5.1 Next-generation hybrid multiscale modeling

Improved multiscale and hybrid mathematics and computational techniques are necessary for further advances. In the agent-based model, each necrotic cell agent must remain in memory on the order of simulated months; by later times, necrotic agents outnumber viable agents by three to one or more. And yet the vast majority of these objects are engaged in the slow time scale processes of calcification and solid degradation—processes that are well-suited to continuum modeling!

Lowengrub and colleagues are now developing a sophisticated continuum model of necrotic cell calcification in DCIS [17]. We apply a phase field approach [91] to model the tumor as a mixture of fluid, extracellular matrix, and cells. The model can separately track the necrotic and calcified cell fractions. We also include a sophisticated model of the basement membrane, which can deform in response to mechanical stresses introduced by the growing tumor [16]. Preliminary results recapitulate the gross features observed in DCIS pathology: a viable rim of appropriate thickness surrounding a necrotic core with a calcified center [17]. See Fig. 14.

Fig. 14 Preliminary continuum simulation of solid-type DCIS with comedonecrosis and calcifications [17]. **Legend:** Green curve: deformed basement membrane. Red curve: viable tumor boundary. Magenta curve: calcified necrotic debris. White shading: non-calcified necrotic tissue.
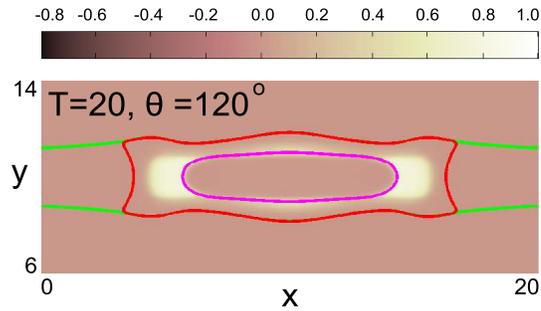
We plan to integrate these discrete and continuum approaches in a hybrid model, as outlined in [43, 50]. A key issue is determining the rate constants for the continuum model. As water loss in necrotic cells does not occur at a fixed rate, it may be best to simulate using the discrete model until most fluid has been lost, then "convert mass" to the continuum model for the slower time scale processes. A more detailed analysis of the full agent-based model could yield the correct average per-volume rate of volume loss in the necrotic tissues, similarly to the upscaling approach we developed in [23, 54]. Other approaches may include introduction of an age structuring variable, as is often used today in mathematical ecology (e.g., [5, 41, 49]).

5.2 A vision for quantitative, integrative computational oncology

An integrative modeling approach—where clinicians, modelers, and biologists work in close-knit teams throughout the modeling process—is necessary to push computational oncology towards clinical application. Conversely, just as the space race in the 1950s and 1960s fueled advances throughout engineering, physics, and mathematics, efforts to push the envelope in patient-specific modeling are advancing the state-of-the-art in mathematical modeling, computational algorithms, experimental methods, and clinical practice. Moreover, quantitatively and explicitly stating our working biological hypotheses gives us the opportunity to rigorously and systematically test and refine what can best be described as *current cancer biology orthodoxy*. We close this chapter by outlining our vision of clinically-oriented integrative computational oncology, and its possible impact beyond the clinic.

Model Design: Clinicians and modelers jointly identify important unanswered clinical questions. This helps modelers avoid investigating unnecessary tangents while bringing fresh perspective to the clinicians. Biologists help modelers identify working hypotheses around which to build their models. While explicitly writing these out and "translating" them to code, we can evaluate what is and is not truly known in cancer biology. Lastly, while developing the model and numerical algorithms, assessing the expected clinical and experimental data helps in choosing the modeling approach; the model may expose needs for additional experimental measurements.

Data generation, model calibration, and early testing: Modelers and clinicians jointly plan studies and choose which clinical data to gather (pathology, radiology, case histories, etc.). Biologists and modelers jointly plan experiments to supplement the clinical data and inform the model's constitutive relations. These data are integrated into the model with the help of statisticians, image processing specialists, and others. Early simulations help test and refine the data, model, and calibration.

Simulation, analysis, validation, and feedbacks: The calibration procedure is applied to simulate cancer in individual patients. The simulation data are postprocessed, yielding quantitative predictions that we validate for each patient. This quantitative focus allows us to assess and improve our underlying biological hypotheses. If the predictions are accurate, trials may be planned to assess the model's ability to assist individual treatment decisions. The modelers, clinicians, and biologists jointly identify future refinements and experiments. They also jointly select new modeling foci as suggested by both clinical needs and model-derived insights.

5.2.1 Application of integrative modeling to breast cancer

This approach guides our work on breast cancer. We have built a team that now includes oncologists, pathologists, radiologists, biologists and modelers [63], and we are continuing to recruit complementary expertise (e.g., in analytical pathology, tissue bioengineering, etc.). We have jointly identified that patient-specific predic-

tions of progression from *in situ* to invasive carcinoma would be of immense clinical value, and would naturally build upon our increasingly accurate *in situ* models. To that end, we are developing key modeling technologies, such as improved BM and ECM mechanics [20] and multiscale matrix metalloproteinase transport-reaction kinetics [19]. Early modeling results will help guide future experimental design.

Given the critical role of tissue necrosis in DCIS progression, we are developing next-generation models of intracellular fluid transport, solid synthesis, and dystrophic calcification to more accurately describe individual cell volume and composition changes during these processes [64], based upon *in vitro* measurements we are currently gathering [68]. By this approach, it should soon be possible to accurately simulate common pathology stains based upon each cell agent's composition. This, in turn, should make possible new and innovative quantitative comparisons to patient pathology, better refinement of the otherwise nigh-unmeasurable necrosis time scales, and ultimately more accurate predictions of clinical progression.

The interested reader can find up-to-date information on these efforts (including frequent news postings, animations, tutorials, simulation data, and software) at MathCancer.org. We also encourage the interested reader to visit the newly-established *Consortium for Integrative Computational Oncology* at the University of Southern California, where we are developing this approach with a focus on building community and training the next generation of interdisciplinary cancer scientists.

5.2.2 Broader implications and spillover benefits

The quest for quantitative accuracy in patient-specific modeling drives advances in mechanistic modeling. Quantitative testing allows us to choose among competing models, where multiple models may be qualitatively compelling, but fewer are quantitatively reasonable. To the extent that rigorously-calibrated models can successfully make quantitative predictions in individual patients, we gain new confidence in the underlying models. Because the models are built to be universal (cancer cells are just cells with different phenotypic parameter values), these advances will be of use across computational biology. Likewise, efficient numerical simulation of these increasingly sophisticated models is driving advances in applied parallel computing and hybrid and multiscale modeling. Any derived algorithms will be of benefit across applied mathematics and engineering.

If we should reach the point where we can integrate *in vitro* measurements with clinical data to accurately predict cancer progression and therapy response in individual patients, the implications are vast: new insights from wetlab biology could be immediately evaluated for potential impact in individual patients in combination with current therapies, offering accelerated discovery and clinical translation. Ultimately, it is our goal that this approach will help bridge the gap between theoretical modeling, wetlab biology, and clinical practice to develop and deliver patient-calibrated predictive tools. We believe that such tools will one day help clinicians and their patients to make optimal, personalized treatment decisions that incorporate both accepted clinical practice and cutting-edge research results.

Acknowledgements

References

1. Altman, D.A., Atkinson, D.S., Brat, D.J.: Glioblastoma multiforme. Radiographics **27**(3), 883–88 (2007)
2. Anderson, A.R.A.: A hybrid mathematical model of solid tumour invasion: the importance of cell adhesion. Math. Med. Biol. **22**(2), 163–86 (2005)
3. Ayre, K.J., Hulbert, A.J.: Dietary fatty acid profile influences the composition of skeletal muscle phospholipids in rats. J. Nutr. **126**(3), 653–62 (1996)
4. Bacsó, Z., Everson, R.B., Eliason, J.F.: The DNA of annexin V-binding apoptotic cells is highly fragmented. Cancer Research **60**(16), 4623 (2000)
5. Bai, Z.: A periodic age-structured epidemic model with a wide class of incidence rates. J. Math. Anal. Appl. **393**(2), 367–76 (2012)
6. Barros, L.F., Hermosilla, T., Castro, J.: Necrotic volume increase and the early physiology of necrosis. Comp. Biochem. Physiol. A. Mol. Integr. Physiol. **130**(3), 401–9 (2001)
7. Barros, L.F., Kanaseki, T., Sabriov, R., Morishima, S., Castro, J., Bittner, C.X., Maeno, E., Ando-Akatsuka, Y., Okada, Y.: Apoptotic and necrotic blebs in epithelial cells display similar neck diameters but different kinase dependency. Cell Death Diff. **10**(6), 687–97 (2003)
8. Basanta, D., Strand, D.W., Lukner, R.B., Franco, O.E., Cliffel, D.E., Ayala, G.E., Hayward, S.W., Anderson, A.R.A.: The role of transforming growth factor-β mediated tumor-stroma interactions in prostate cancer progression: An integrative approach. Canc. Res. **69**(17), 7111–20 (2009)
9. Basu, S., Binder, R.J., Suto, R., Anderson, K.M., Srivastava, P.K.: Necrotic but not apoptotic cell death releases heat shock proteins, which deliver a partial maturation signal to dendritic cells and activate the NF-κB pathway. Int. Immunol. **12**(11), 1539–46 (2000)
10. Blagosklonny, M.V., Robey, R., Bates, S., Fojo, T.: Pretreatment with DNA-damaging agents permits selective killing of checkpoint-deficient cells by microtubule-active drugs. J. Clin. Investigation **105**(4), 533–9 (2000)

11. Buerger, H., Mommers, E.C., Littmann, R., Diallo, R., Brinkschmidt, C., Poremba, C., Dockhorn-Dworniczak, B., van Diest, P.J., Böcker, W.B.: Correlation of morphologic and cytogenetic parameters of genetic instability with chromosomal alterations in in situ carcinomas of the breast. Am. J. Clin. Pathol. **114**, 854–9 (2000)

12. Byrne, H., Chaplain, M.A.J.: Necrosis and apoptosis: Distinct cell loss mechanisms in a mathematical model of avascular tumour growth. J. Theor. Med. **1**(3), 223–35 (1998)

13. Byrne, H., Preziosi, L.: Modelling solid tumour growth using the theory of mixtures. Math. Med. Biol. **20**(4), 341–66 (2003)

14. Cantoni, O., Guidarelli, A., Palomba, L., Fiorani, M.: U937 cell necrosis mediated by peroxynitrite is not caused by depletion of ATP and is prevented by arachidonate via an ATP-dependent mechanism. Mol. Pharm. **67**(5), 1399–1405 (2005)

15. Carlson, K.L., Helvie, M.A., Roubidoux, M.A., Kleer, C.G., Oberman, H.A., Wilson, T.E., Pollack, E.W., Rochester, A.B.: Relationship between mammographic screening intervals and size and histology of ductal carcinoma in situ. Am. J. Roentenology **172**(2), 313–7 (1999)

16. Chen, Y.: Modeling tumor growth in complex, dynamic geometries. Ph.D. dissertation, University of California, Irvine Department of Mathematics (2012)

17. Chen, Y., Lowengrub, J.S.: Tumor growth in complex, evolving geometries: A diffuse domain approach (2012). (in preparation)

18. Cristini, V., Lowengrub, J.S., Nie, Q.: Nonlinear simulation of tumor growth. J. Math. Biol. **46**(3), 191–224 (2003)

19. D'Antonio, G., Macklin, P.: A multiscale hybrid discrete-continuum model of matrix metalloproteinase transport and basement membrane-extracellular matrix degradation (2012). (in preparation)

20. D'Antonio, G., Macklin, P., Preziosi, L.: An agent-based model for elasto-plastic mechanical interactions between cells, basement membrane and extracellular matrix. Math. Biosci. Eng. (2012). URL http://MathCancer.org/Publications.php#dantonio12_mbe. (in review)

21. Drasdo, D., Höhme, S.: A single-scale-based model of tumor growth *in vitro*: monolayers and spheroids. Phys. Biol. **2**(3), 133–47 (2005)

22. Drasdo, D., Kree, R., McCaskill, J.S.: Monte-carlo approach to tissue cell populations. Phys. Rev. E **52**(6), 6635–57 (1995)

23. Edgerton, M.E., Chuang, Y.L., Macklin, P., Yang, W., Bearer, E.L., Cristini, V.: A novel, patient-specific mathematical pathology approach for assessment of surgical volume: Application to ductal carcinoma in situ of the breast. Anal. Cell. Pathol. **34**(5), 247–63 (2011)

24. Eichbaum, C., Meyer, A.S., Wang, N., Bischofs, E., Steinborn, A., Bruckner, T., Brodt, P., Sohn, C., Eichbaum, M.H.R.: Breast cancer cell-derived cytokines, macrophages and cell adhesion: Implications for metastasis. Anticanc. Res. **31**(10), 3219–27 (2011)

25. Elmore, S.: Apoptosis: A review of programmed cell death. Toxicologic Pathol. **35**(4), 495–516 (2007)

26. Erez, N., Truitt, M., Olson, P., Hanahan, D.: Cancer-associated fibroblasts are activated in incipient neoplasia to orchestrate tumor-promoting inflammation in an NF-κB-dependent manner. Canc. Cell **17**(2), 135–47 (2010)

27. Evans, A.: The diagnosis and management of pre-invasive breast disease: Radiological diagnosis. Breast Canc. Res. **5**(5), 250–3 (2003)

28. Evans, A., Clements, K., Maxwell, A., Bishop, H., Handby, A., Lawrence, G., Pinder, S.E.: Lesion size is a major determinant of the mammographic features of ductal carcinoma *in situ*: Findings from the Sloane project. Radiol. **53**(3), 181–4 (2010)

29. Evans, A., Pinder, S., Wilson, R., Sibbering, M., Poller, D., Elston, C., Ellis, I.: Ductal carcinoma in situ of the breast: correlation between mammographic and pathologic findings. Am. J. Roentgen. **162**(6), 1307–11 (1994)

30. Fall, C.P., Bennett, J.P.: Characterization and time course of MPP+-induced apoptosis in human SH-SY5Y neuroblastoma cells. J. Neuros. Res. **55**(5), 620–8 (1999)

31. Festjens, N., Berghe, T.V., Vandenabeele, P.: Necrosis, a well-orchestrated form of cell demise: Signalling cascades, important mediators and concomitant immune response. Biochimica et Biophysica Acta - Bioenergetics **1757**(9–10), 1371–87 (2006)

32. Fesus, L.: Transglutaminase-catalyzed protein cross-linking in the molecular program of apoptosis and its relationship to neuronal processes. Cell. Molec. Neurobiol. **18**, 683–94 (1998)
33. Frieboes, H.B., Zheng, X., Sun, C.H., Tromberg, B., Gatenby, R., Cristini, V.: An integrated computational/experimental model of tumor invasion. Canc. Res. **66**(3), 1597–604 (2006)
34. Gadeau, A.P., Chaulet, H., Daret, D., Kockx, M., Daniel-Lamaziè, J.M., Desgranges, C.: Time course of osteopontin, osteocalcin, and osteonectin accumulation and calcification after acute vessel wall injury. J. Histochem. Cytochem. **49**(1), 79–86 (2001)
35. Galle, J., Loeffler, M., Drasdo, D.: Modeling the effect of deregulated proliferation and apoptosis on the growth dynamics of epithelial cell populations in vitro. Biophys. J. **88**(1), 62–75 (2005)
36. Garland, J.M., Halestrap, A.: Energy metabolism during apoptosis. J. Biol. Chem. **272**(8), 4680–8 (1997)
37. Grivennikov, S.I., Greten, F.R., Karin, M.: Immunity, inflammation, and cancer. Cell **140**(6), 883–99 (2010)
38. Hengartner, M.O.: The biochemistry of apoptosis. Nature **407**(6805), 770–6 (2000)
39. Hofvind, S., Iversen, B.F., Eriksen, L., Styr, B.M.S., Kjellevold, K., Kurz, K.D.: Mammographic morphology and distribution of calcifications in ductal carcinoma *in situ* diagnosed in organized screening. Acta Radiologica **52**(5), 481–7 (2011)
40. Huether, S., McCance, K.: Understanding Pathology, 5 edn., chap. 3. Mosby, St. Louis, MO USA (2011)
41. Iannelli, M., Ripoll, J.: Two-sex age structured dynamics in a fixed sex-ratio population. Nonlinear Analysis: Real World Applications **13**(6), 2562–77 (2012)
42. Jian, B., Narula, N., Li, Q.Y., Mohler III, E.R., Levy, R.J.: Progression of aortic valve stenosis: TGF-β1 is present in calcified aortic valve cusps and promotes aortic valve interstitial cell calcification via apoptosis. Ann. Thoracic Surg. **75**(2), 457–65 (2003)
43. Jin, F., Chuang, Y.L., Cristini, V., Lowengrub, J.S.: Hybrid continuum-discrte tumor models. In: V. Cristini and J.S. Lowengrub, Multiscale modeling of cancer, chap. 8, pp. 153–82. Cambridge University Press, Cambridge, UK (2010)
44. Kerr, J.F.R., Winterford, C.M., Harmon, B.V.: Apoptosis. its significance in cancer and cancer therapy. Cancer **73**(8), 2013–26 (1994)
45. Krause, R.F., Beamer, K.C.: Lipid content and phospholipid metabolism of subcellular fractions from testes of control and retinol-deficient rats. J. Nutr. **104**(5), 629–37 (1974)
46. Krysko, D.V., Berghe, T.V., D'Herde, K., Vandenabeele, P.: Apoptosis and necrosis: Detection, discrimination and phagocytosis. Methods **44**(3), 205–21 (2008)
47. Kumar, V., Abbas, A.K., Aster, J.C., Fausto, N.: Pathologic Basis of Disease, 8 edn., chap. 1. Saunders Elsevier, Philadelphia, PA USA (2009)
48. Lee, J.S., Basalyga, D.M., Simionescu, A., Isenburg, J.C., Sinionescu, D.T., Vyavahare, N.R.: Elastin calcification in the rate subdermal model is accompanied by up-regulation of degradative and osteogenic cellular responses. Am. J. Pathol. **168**(2), 490–8 (2006)
49. Levin, S.A., Goodyear, C.P.: Analysis of an age-structured fishery model. J. Math. Biol. **9**, 245–74 (1980)
50. Lowengrub, J.S., Frieboes, H.B., Jin, F., Chuang, Y.L., Li, X., Macklin, P., Wise, S.M., Cristini, V.: Nonlinear modeling of cancer: Bridging the gap between cells and tumors. Nonlinearity **23**(1), R1–R91 (2010)
51. Macklin, P.: Numerical simulation of tumor growth and chemotherapy. M.S. thesis, University of Minnesota School of Mathematics (2003)
52. Macklin, P.: Biological background. In: V. Cristini and J.S. Lowengrub, Multiscale modeling of cancer, chap. 2, pp. 8–24. Cambridge University Press, Cambridge, UK (2010)
53. Macklin, P.: Basic ductal carcinoma in situ (DCIS) pathobiology for modelers (2012). URL http://MathCancer.org/Resources.php#DCIS_biology_tutorial. (online tutorial)
54. Macklin, P., Edgerton, M.E., Cristini, V.: Agent-based cell modeling: application to breast cancer. In: V. Cristini and J.S. Lowengrub, Multiscale modeling of cancer, chap. 10, pp. 216–244. Cambridge University Press, Cambridge, UK (2010)

55. Macklin, P., Edgerton, M.E., Lowengrub, J., Cristini, V.: Discrete cell modeling. In: V. Cristini and J.S. Lowengrub, Multiscale modeling of cancer, chap. 6, pp. 92–126. Cambridge University Press, Cambridge, UK (2010)

56. Macklin, P., Edgerton, M.E., Thompson, A.M., Cristini, V.: Patient-calibrated agent-based modelling of ductal carcinoma in situ (DCIS): From microscopic measurements to macroscopic predictions of clinical progression. J. Theor. Biol. **301**, 122–40 (2012)

57. Macklin, P., Kim, J., Tomaiuolo, G., Edgerton, M.E., Cristini, V.: Agent-based modeling of ductal carcinoma in situ: Application to patient-specific breast cancer modeling. In: T. Pham (ed.) Computational Biology: Issues and Applications in Oncology, chap. 4, pp. 77–112. Springer (2009)

58. Macklin, P., Lowengrub, J.S.: Evolving interfaces via gradients of geometry-dependent interior poisson problems: application to tumor growth. J. Comput. Phys. **203**(1), 191–220 (2005)

59. Macklin, P., Lowengrub, J.S.: An improved geometry-aware curvature discretization for level set methods: application to tumor growth. J. Comput. Phys. **215**(2), 392–401 (2006)

60. Macklin, P., Lowengrub, J.S.: Nonlinear simulation of the effect of microenvironment on tumor growth. J. Theor. Biol. **245**(4), 677–704 (2007)

61. Macklin, P., Lowengrub, J.S.: A new ghost cell/level set method for moving boundary problems: Application to tumor growth. J. Sci. Comp. **35**(2–3), 266–99 (2008)

62. Macklin, P., McDougall, S., Anderson, A.R.A., Chaplain, M.A.J., Cristini, V., Lowengrub, J.: Multiscale modeling and nonlinear simulation of vascular tumour growth. J. Math. Biol. **58**(4–5), 765–98 (2009)

63. Macklin, P., Mumenthaler, S., Jordan, L.B., Purdie, C.A., Evans, A.J., Thompson, A.M.: Integration of pathology, radiology, and in vitro data in patient-calibrated cancer simulations: Recent advances and future outlook for ductal carcinoma in situ (DCIS). To be presented at: Annual Meeting of the Society for Mathematical Biology (SMB) (2012,accepted). URL http://www.mathcancer.org/publications/macklin12_SMB.pdf

64. Macklin, P., et al.: Agent-based cell modeling with improved subcellular fluid and solid transport: comparison with ductal carcinoma in situ pathology (2012). (in preparation)

65. Majno, G., Joris, I.: Apoptosis, oncosis, and necrosis. an overview of cell death. Am. J. Pathol. **146**(1), 3–15 (1995)

66. Majno, G., Joris, I.: Cells, Tissues, and Disease: Principles of General Pathology, second edn. Oxford University Press, New York (2004)

67. McCarthy, J.V., Cotter, T.G.: Cell shrinkage and apoptosis: a role for potassium and sodium ion efflux. Cell Death Diff. **4**(8), 756–70 (1997)

68. Mumenthaler, S., Macklin, P., et al.: Time-course volume and water fraction measurements in cycling and apoptotic breast cancer cell lines (2012). (in preparation)

69. Muttarak, M., Kongmebhol, P., Sukhamwang, N.: Breast calcifications: which are malignant? Singapore Med. J. **50**(9), 907–13 (2009)

70. Noch, E., Khalili, K.: Molecular mechanisms of necrosis in glioblastoma: The role of glutamate excitotoxicity. Canc. Biol. and Ther. **8**(19), 1791–7 (2009)

71. Norton, K.A., Wininger, M., Bhanot, G., Ganesan, S., Barnard, N., Shinbrot, T.: A 2D mechanistic model of breast ductal carcinoma in situ (DCIS) morphology and progression. J. Theor. Biol. **263**(4), 393–406 (2010)

72. Ottesen, G.L., Christensen, I.J., Larsen, J.K., Larsen, J., Baldetorp, B., Linden, T., Hansen, B., Andersen, J.: Carcinoma in situ of the breast: correlation of histopathology to immunohistochemical markers and DNA ploidy. Breast Canc. Res. Treat. **60**(3), 219–26 (2000)

73. Owen, M.R., Byrne, H.M., Lewis, C.E.: Mathematical modelling of the use of macrophages as vehicles for drug delivery to hypoxic tumour sites. J. Theor. Biol. **226**(4), 377–91 (2004)

74. Pearson, O.H., Manni, A., Arafah, B.M.: Antiestrogen treatment of breast cancer: An overview. Canc. Res. **42**(8 Suppl.), 3424s–8s (1982)

75. Ramis-Conde, I., Drasdo, D., Anderson, A.R.A., Chaplain, M.A.J.: Modeling the influence of the e-cadherin-beta-catenin pathway in cancer cell invasion: A multiscale approach. Biophys. J. **95**(1), 155–165 (2008)

76. Richards, C.H., Mohammed, Z., Qayyum, T., Horgan, P.G., McMillan, D.C.: The prognostic value of histological tumor necrosis in solid organ malignant disease: a systematic review. Future Oncol. **7**(10), 1223–35 (2011)

77. Richards, C.H., Roxburgh, C.S.D., Anderson, J.H., McKee, R.F., Foulis, A.K., Horgan, P.G., McMillan, D.C.: Prognostic value of tumour necrosis and host inflammatory responses in colorectal cancer. Brit. J. Surgery **99**(2), 287–94 (2012)

78. de Roos, M.A.J., Pijnappel, R.M., Post, W.J., de Vries, J., Baas, P.C., Groote, L.D.: Correlation between imaging and pathology in ductal carcinoma in situ of the breast. World J. Surg. Onco. **2**(1), 4 (2004)

79. Rüegg, C.: Leukocytes, inflammation, and angiogenesis in cancer: fatal attractions. J. Leukocyte Biol. **80**(4), 682–4 (2006)

80. Scarlett, J.L., Sheard, P.W., Hughes, G., Ledgerwood, E.C., Ku, H.K., Murphy, M.P.: Changes in mitochondrial membrane potential during staurosporine-induced apoptosis in Jurkat cells. FEBS Letters **475**(3), 267–72 (2000)

81. Seymour, H.R., Cooke, J., Given-Wilson, R.M.: The significance of spontaneous resolution of breast calcification. Brit. J. Radiol. **72**(853), 3–8 (1999)

82. Sickles, E.A.: Mammographic features of 300 consecutive nonpalpable breast cancers. Am. J. Roentgen. **146**(4), 661–3 (1986)

83. Silva, A.S., Gatenby, R.A., Gillies, R.J., Yunes, J.A.: A quantitative theoretical model for the development of malignancy in ductal carcinoma in situ. J. Theor. Biol. **262**(4), 601–613 (2010)

84. Silverstein, M.J., Lagios, M.D., Craig, P.H., Waisrnan, J.R., Lewinsky, B.S., Colburn, W.J., Poller, D.N.: A prognostic index for ductal carcinoma in situ of the breast. Cancer **77**(11), 2267–74 (1996)

85. Stomper, P.C., Connolly, J.L., Meyer, J.E., Harris, J.R.: Clinically occult ductal carcinoma in situ detected with mammography: analysis of 100 cases with radiologic-pathologic correlation. Radiology **172**(1), 235–41 (1989)

86. Thomson, J.Z., Evans, A.J., Pinder, S.E., Burrell, H.C., Wilson, A.R.M., Ellis, I.O.: Growth pattern of ductal carcinoma in situ (DCIS): a retrospective analysis based on mammographic findings. Br. J. Canc. **85**(2), 225–7 (2001)

87. Trump, B.E., Berezesky, I.K., Chang, S.H., Phelps, P.C.: The pathways of cell death: Oncosis, apoptosis, and necrosis. Toxicologic Pathology **25**(1), 82–8 (1997)

88. Walsh, G.M.: Mechanisms of human eosinophil survival and apoptosis. Clin. Exper. Allergy **27**(5), 482–7 (1997)

89. Ward, J.P., King, J.R.: Mathematical modelling of avascular tumour growth. IMA J. Math. Appl. Medicine Biol. **14**(1), 36–69 (1997)

90. Ward, J.P., King, J.R.: Mathematical modelling of avascular-tumour growth II: modelling growth saturation. Math. Med. Biol. **16**(2), 171–211 (1999)

91. Wise, S.M., Lowengrub, J.S., Frieboes, H.B., Cristini, V.: Three-dimensional multispecies nonlinear tumor growth–I. model and numerical method. J. Theor. Biol. **253**(3), 524–43 (2008)

92. Yagata, H., Harigaya, K., Suzuki, M., Nagashima, T., Hashimoto, H., Ishii, G., Miyazaki, M., Nakajima, N., Mikata, A.: Comedonecrosis is an unfavorable marker in node-negative invasive breast carcinoma. Pathol. Internatl. **53**(8), 501–6 (2003)

93. Zheng, X., Wise, S.M., Cristini, V.: Nonlinear simulation of tumor necrosis, neovascularization and tissue invasion via an adaptive finite-element/level set method. Bull. Math. Biol. **67**(2), 211–59 (2005)